

Probing the Origins of the C IV and Fe K α Baldwin Effects

Jian Wu¹, Daniel E. Vanden Berk^{1,2}, W. N. Brandt¹, Donald P. Schneider¹, Robert R. Gibson^{1,3},
and
Jianfeng Wu¹

jwu@astro.psu.edu

ABSTRACT

We use UV/optical and X-ray observations of 272 radio-quiet Type 1 AGNs and quasars to investigate the C IV Baldwin Effect (BEff). The UV/optical spectra are drawn from the *Hubble Space Telescope*, *International Ultraviolet Explorer* and Sloan Digital Sky Survey archives. The X-ray spectra are from the *Chandra* and *XMM-Newton* archives. We apply correlation and partial-correlation analyses to the equivalent widths, continuum monochromatic luminosities, and α_{ox} , which characterizes the relative X-ray to UV brightness. The equivalent width of the C IV $\lambda 1549$ emission line is correlated with both α_{ox} and luminosity. We find that by regressing $l_{\nu}(2500 \text{ \AA})$ with EW(C IV) and α_{ox} , we can obtain tighter correlations than by regressing $l_{\nu}(2500 \text{ \AA})$ with only EW(C IV). Both correlation and regression analyses imply that $l_{\nu}(2500 \text{ \AA})$ is not the only factor controlling the changes of EW(C IV); α_{ox} (or, equivalently, the soft X-ray emission) plays a fundamental role in the formation and variation of C IV. Variability contributes at least 60% of the scatter of the EW(C IV)- $l_{\nu}(2500 \text{ \AA})$ relation and at least 75% of the scatter of the of the EW(C IV)- α_{ox} relation.

In our sample, narrow Fe K α 6.4 keV emission lines are detected in 50 objects. Although narrow Fe K α exhibits a BEff similar to that of C IV, its equivalent width has almost no dependence on either α_{ox} or EW(C IV). This suggests that the majority of narrow Fe K α emission is unlikely to be produced in the broad emission-line region. We do find suggestive correlations between the emission-line luminosities of C IV and Fe K α , which could be potentially used to estimate the detectability of the Fe K α line of quasars from rest-frame UV spectroscopic observations.

Subject headings: quasars: emission lines

¹Department of Astronomy & Astrophysics, the Pennsylvania State University, 525 Davey Lab, University Park, PA, 16802, USA

²Department of Physics, Saint Vincent College, 300 Fraser-Purchase Road, Latrobe, PA, 15650, USA

³Department of Astronomy, University of Washington, Box 351580, Seattle, WA, 98195, USA

1. Introduction

One of the important properties of AGNs is the relation between the emission-line strength, characterized by the equivalent width (EW), and continuum luminosity, because it reveals that the regions emitting these two spectral components are associated. Baldwin (1977a) found that the EW of C IV $\lambda 1549$ (C IV) is inversely correlated with the quasar monochromatic luminosity at 1450 Å, $l_{\lambda}(1450 \text{ Å})$, namely, $\log \text{EW}(\text{C IV}) = k \log l_{\nu}(1450 \text{ Å}) + b$. Carswell & Smith (1978) referred to this trend as the “Baldwin Effect” (BEff), a designation now widely used to describe line strength-luminosity relations. Baldwin (1977a) identified this relation using only 20 quasi-stellar objects with $29.8 \lesssim \log l_{\nu}(1450 \text{ Å}) \lesssim 32.0$ and $1.24 < z < 3.53$. Subsequent UV/optical surveys have enabled investigation of this relation with wider luminosity and redshift ranges (e.g., Kinney, Rivolo & Koratkar 1990; Zamorani et al. 1992). It has been found that the BEff exists for not only C IV but many other broad emission lines such as Ly α , C III] $\lambda 1908$, Si IV $\lambda 1396$, Mg II $\lambda 2798$ (Dietrich et al. 2002; Vanden Berk et al. 2009, in preparation), UV iron emission lines (Green, Forster & Kuraszkievicz 2001), and even forbidden lines such as [O II] $\lambda 3727$ and [Ne V] $\lambda 3426$ (Croom et al. 2002). Applying a spectral-composite technique (Vanden Berk et al. 2001) to the Sloan Digital Sky Survey (SDSS; York et al. 2000) Data Release Three (DR3) quasar catalog (Schneider et al. 2005), Vanden Berk et al. (2009, in preparation) found that the BEff evolves with redshift, which is a source of scatter in this relation for a sample with a wide range of redshift.

The X-ray BEff (or Fe K α BEff), in which the EW of the narrow Fe K α line at 6.4 keV (hereafter abbreviated to Fe K α) is anti-correlated with X-ray luminosity, $l_{\nu}(2 \text{ keV})$, was discovered in the early 1990s from observations by the X-ray observatory *Ginga* (Iwasawa & Taniguchi 1993). This relation has been subsequently confirmed using data from *ASCA* (Tanaka, Inoue & Holt 1994; Nandra et al. 1997) and from *Chandra* and *XMM-Newton* (Page et al. 2004; Zhou & Wang 2005; Jiang et al. 2006; Bianchi et al. 2007). Possible sites of origin for narrow Fe K α emission include the broad emission-line region (BELR), the outskirts of the accretion disk, and the molecular torus (e.g., Weaver et al. 1992, Antonucci 1993; Krolik, Madau & Zycki 1994).

Although it is well accepted that the BEff exists for many UV/optical emission lines (e.g., Osmer & Shields 1999; Shields 2007), there is currently no theoretical model that provides a compelling and complete explanation of this well-known phenomenon. Several physical explanations have been proposed to account for the UV/optical BEff.

One promising explanation is that the continuum shape may be luminosity dependent. In this model, the UV/optical BEff is due to the softening of the spectral energy distribution (SED) at high luminosity, which lowers the ion populations having high ionization potentials (Netzer, Laor & Gondhalekar 1992; Korista, Baldwin & Ferland 1998). It has been found, using *Einstein Observatory* data, that the quasar SED, parameterized by α_{ox} ¹ (Tananbaum et al. 1979), depends on UV luminos-

¹Defined as $\alpha_{\text{ox}} = \log [l_{\nu}(2 \text{ keV})/l_{\nu}(2500 \text{ Å})] / \log [\nu(2 \text{ keV})/\nu(2500 \text{ Å})] = 0.3838 \log [l_{\nu}(2 \text{ keV})/l_{\nu}(2500 \text{ Å})]$. α_{ox} is used to characterize the spectral hardness in the UV to X-ray band (e.g., Avni & Tananbaum 1982, 1986; Anderson

ity (e.g., Zamorani et al. 1981). Later research using radio-quiet (RQ) optically selected quasar samples from the SDSS Early Data Release (Stoughton et al. 2002) confirmed and extended this result (e.g., Vignali, Brandt & Schneider 2003). Using optically selected AGNs Strateva et al. (2005) and Steffen et al. (2006) firmly established the correlation of α_{ox} with UV luminosity for these sources. The idea that the UV/optical BEff is attributable to SED-driven ionization effects is supported both observationally (Zheng & Malkan 1993; Green 1996, 1998) and theoretically (Netzer, Laor & Gondhalekar 1992). Recent work on a sample of non-Broad Absorption Line (BAL), radio-quiet, optically selected quasars indicates that the EW of C IV depends both on UV and X-ray luminosity. The physics of the C IV BEff is apparently associated with both UV and X-ray emission (e.g., Gibson, Brandt & Schneider, 2008, hereafter GBS08, and references therein).

Other proposed BEff drivers include the Eddington ratio, L/L_{Edd} (Baskin & Laor 2004; Bachev et al. 2004; Warner, Hamann & Dietrich 2004; Zhou & Wang 2005), the black-hole mass (Netzer, Laor & Gondhalekar 1992; Wandel, Peterson & Malkan 1999; Shields 2007), and the luminosity dependence of metallicity (Warner, Hamann & Dietrich 2004).

In this paper we investigate the origin of the BEff for the C IV emission line in a sample of 272 Type 1 AGNs and quasars. Although C IV is not the only UV/optical broad emission line that exhibits a BEff, we selected it to study this phenomenon not only because it is a representative and well-accepted BEff emission line, but also because C IV resides in a relatively clean spectral region where the local continuum can be well approximated as a single power-law, with few blends with other emission lines (in particular the iron emission forest) and limited contamination from the AGN host galaxy. These properties make it relatively straightforward to perform spectral fitting and obtain accurate emission-line parameters for C IV. We also use partial-correlation analysis (PCA) and linear-regression regression analysis to investigate the correlations between EW, monochromatic luminosity, and α_{ox} for C IV and narrow Fe K α emission lines.

Over the past three decades, there have been a large number of studies of the BEff. Our work on the C IV/Fe K α lines combines the following important features (1) a wide range in redshift ($0.009 \lesssim z \lesssim 4.720$) and luminosity ($27.81 \lesssim \log l_{\nu}(2500 \text{ \AA}) \lesssim 33.04$) that allows one to disentangle evolutionary vs. luminosity, so that we are not narrowing our study for quasars with a particular luminosity or at a certain redshift; (2) a relatively large sample size (272 objects); (3) the use of partial correlation analysis; and (4) a high X-ray detection rate ($\sim 94\%$); and (5) estimates of the effects of observational errors and object variability.

We describe the sample selection in § 2 and the methods used to process the data in § 3. In § 4, we perform partial-correlation and linear-regression analyses to investigate the roles of α_{ox} in the C IV and Fe K α BEffs. In § 5, we probe the connections between C IV and Fe K α relationships in EWs, fluxes and luminosities. We present our conclusions in § 6. Throughout this work, we

& Margon 1987; Wilkes et al. 1994; Vignali, Brandt & Schneider 2003; Strateva et al. 2005; Steffen et al. 2006; Just et al. 2007).

adopt the following cosmology: $\Omega_M = 0.3$, $\Omega_\Lambda = 0.7$, $H_0 = 70 \text{ km s}^{-1} \text{ Mpc}^{-1}$.

2. Sample Construction

The quasar sample in our study is drawn from three sources: 50 objects from Jiang et al. (2006), which will be referred to as “Sample A”; 98 objects from GBS08, which will be referred to as “Sample B”; and 124 objects from Just et al. (2007), which is referred to as “Sample C”. We define our “combined sample” as the combination of these three data sets.

2.1. Sample A

Jiang et al. (2006) compiled a dataset of 101 Type 1 AGNs with Fe K α observations from both the *Chandra* and *XMM-Newton* archives. The detection fraction of the Fe K α line in their combined sample is around 55%. The redshifts of the AGNs range from 0.003 to 3.366, but most of the objects (87%) are low-redshift ($z \lesssim 0.4$) AGNs. The monochromatic luminosities, $l_\nu(2500 \text{ \AA})$, range from $10^{26.0}$ to $10^{31.5} \text{ erg s}^{-1} \text{ Hz}^{-1}$. We chose this dataset because it is the most complete Fe K α BEff sample with high-quality data obtained from the most sensitive X-ray missions. However, because the number of AGNs observed in the X-ray band is much smaller than the number observed optically and not all X-ray observed AGNs present Fe K α emission lines, the Fe K α sample is significantly limited in size.

We searched for UV/optical spectra of all 101 objects from the archival databases for *HST* and *IUE*. We found 82 spectra covering the wavelength region around the C IV emission line (containing at least the 1500–1600 \AA band). If observations are available from both *HST* and *IUE*, we selected the *HST* observations due to their generally higher signal-to-noise (S/N) ratio. For spectra with multiple observations using the same instrument, we preferentially use spectra with higher S/N.

Next, we excluded all the radio-loud (RL) objects from the core sample, because additional X-ray emission is produced by the radio jet (e.g., Brinkmann et al. 2000) and changes the value of α_{ox} as well as the slope of the Fe K α BEff.

We further excluded 3 objects for the following reasons:

- *MCG-06-30-15*: The Fe K α profile of MCG-06-30-15 is well fit using a broad disk line model (e.g., Tanaka et al. 1995). The narrow component is not well resolved or very weak. In this work, we only study the narrow component of Fe K α , so this object is excluded.
- *IC 4329a*: The spectrum has low S/N, and the C IV emission line is cannot be accurately measured (e.g., Crenshaw & Kraemer 2001).
- *PG 1407+265*: This object was termed as an “unusual” quasar (McDowell et al. 1995) because it contains extremely weak Ly α and C IV lines. Because of its peculiarity, we exclude

it from our sample.

We removed 5 objects with strong associated absorption lines of C IV $\lambda 1549$: PG 1411+442 (Wise et al. 2004), NGC 4151 (Crenshaw et al. 1999), Ark 564 (Crenshaw et al. 1999), NGC 4051 (Collinge et al. 2001), and PG 1114+445 (Shang et al. 2007). These features prohibit reconstruction of the unabsorbed C IV $\lambda 1549$ emission-line profile. The X-ray absorption associated with the UV line absorption (Brandt, Laor & Wills 2000) might also lead to an under-prediction of continuum flux at 2 keV and, therefore, an incorrect estimation of the intrinsic value of α_{ox} .

Finally, we exclude 8 objects that are classified as Seyfert 1.5 (Sy 1.5) and Sy 1.9² (Osterbrock 1981, 1989). These objects are intermediate between Sy 1 and Sy 2 galaxies and are often subjected to obscuration along the line of sight. Thus their UV, X-ray luminosities and α_{ox} values are also potentially affected.

The final version of Sample A consists of 50 AGNs. Among these objects, 34 are found in the *HST* archive (FOS³ or STIS⁴), and 16 are found in the *IUE* archive (SWP⁵ or LWP⁶). The Fe K α detection rate is 55%, the same as in the entire Jiang et al. (2006) study.

2.2. Sample B

Objects in Sample B were selected from 536 SDSS DR5 (Adelman-McCarthy et al. 2007) quasars in GBS08. These quasars, taken from the DR5 Quasar Catalog (Schneider et al. 2007), are at redshift $1.7 \leq z \leq 2.7$ and have been observed by *Chandra* or *XMM-Newton*. The lower redshift limit ensures that all SDSS spectra in this sample cover the C IV region; the upper redshift limit ensures that the rest-frame flux at 2500 Å is covered so that α_{ox} can be measured accurately.

We excluded the BAL quasars in Table 1 of GBS08. BAL quasars can have strong absorption features in the C IV spectral region that prohibit accurate fitting of the continuum and emission-line profiles. In addition, BALs are usually associated with relatively strong X-ray absorption (e.g., Brandt, Laor & Wills 2000; Gallagher et al. 2006). We only retain objects with *Chandra* observations with angular offsets $< 10'$ to avoid large X-ray flux uncertainties caused by variations of the point spread function. This restriction reduces our sample size to 149. In addition, we excluded RL objects and strong associated absorption-line (AAL) objects. The final version of Sample B consists of 98 objects with $l_{\nu}(2500 \text{ Å})$ between $10^{30.53}$ and $10^{31.67} \text{ erg s}^{-1} \text{ Hz}^{-1}$. This is

²Based on NASA/IPAC Extragalactic Database: <http://nedwww.ipac.caltech.edu/>

³Faint Object Spectrograph

⁴Space Telescope Imaging Spectrograph

⁵Short Wavelength Prime

⁶Long Wavelength Prime

a relatively narrow luminosity range; however, it does provide a significant extension of Sample A since the latter is mostly composed of low-luminosity and low-redshift AGNs.

2.3. Sample C

To examine the relations between α_{ox} , $l_{\nu}(2500 \text{ \AA})$, and $l_{\nu}(2 \text{ keV})$, Just et al. (2007) compiled a sample of 372 objects, including 26 from their core sample, 332 from Steffen et al. (2006), and 14 from Shemmer et al. (2006). BAL quasars, RL quasars, and gravitationally lensed objects have already been excluded from this sample. The gravitationally lensed quasars are removed because their fluxes are strongly amplified and thus their luminosities are uncertain.

Among the 372 objects, 38 are already in Sample A. For the rest of the AGNs, we searched for existing spectra with C IV coverage preferentially from SDSS, then the *HST* and *IUE* archives. Finally, we removed 5 AGNs whose spectra contain strong AALs. These restrictions leave 124 objects in Sample C, in which 91 objects are from the SDSS DR5 quasar catalog, 13 from the *HST* archive, and 20 from the *IUE* archive. The redshift of this sample ranges from 0.015 to 4.720 and $l_{\nu}(2500 \text{ \AA})$ ranges from $10^{28.12}$ to $10^{32.32} \text{ erg s}^{-1} \text{ Hz}^{-1}$.

2.4. Combined Sample

The combined sample (Table 1) consists of a total of 272 objects: 189 (69.5%) have spectra from SDSS, 47 (17.3%) from *HST*, and 36 (13.2%) from *IUE*. The redshifts range from 0.009 to 4.720 (Fig. 1). The gap between $z \sim 0.5$ and $z \sim 1.5$ is caused by instrumentation limitations. Because of the wavelength coverage of the SDSS spectrographs, the redshifts of SDSS quasars having C IV coverage must be greater than 1.5. Most intermediate-redshift AGNs ($0.5 \lesssim z \lesssim 1.5$) are too faint for their UV/optical spectra to be taken by *IUE* and *HST*. Our sample exhibits a strong redshift-luminosity correlation (Fig. 1); we discuss this issue further in our analyses below.

The $l_{\nu}(2500 \text{ \AA})$ of this combined sample ranges between $10^{26.53}$ and $10^{33.04} \text{ erg s}^{-1} \text{ Hz}^{-1}$, including Seyfert galaxies to the most-luminous quasars in the Universe. The X-ray detection rate is 94.9%. The UV properties of the combined sample as well as the UV and X-ray properties of Sample A are tabulated in Table 2 and Table 3. The combined sample will be used to investigate the C IV BEff, while only Sample A will be used to study the Fe K α BEff.

3. Data Processing

3.1. Bad Pixel Removal and Reddening Correction

To ensure that we use high-quality data to perform the continuum and emission-line fitting, we remove bad pixels in the SDSS spectra based on the mask column contained in the SDSS quasar spectral files. We removed all the bad pixels in the spectra of SDSS objects in Sample C.⁷ The excluded pixels cover less than 10% of the total pixels for over 98% of SDSS objects, and the maximum fraction of removed pixels for a single object is 15%.

We perform Galactic reddening corrections to all the spectra using the $E(B-V)$ dependent extinction curve of Fitzpatrick (1999). Values of $E(B-V)$ are calculated following Schlegel, Finkbeiner & Davis (1998).

3.2. Spectral Fitting

3.2.1. Sample A

For each UV/optical spectrum from *HST* or *IUE*, we fit the local continuum in the vicinity of C IV (typically 1300–1700 Å) using a single power-law. We do not expect our measurements to be significantly affected by host-galaxy components because 1) our sample contains only Type I AGNs and quasars in which emission from the nucleus dominates the light from host galaxies in the UV band; and 2) C IV is in the UV region in which the non-nuclear emission primarily arises from massive stars such as O and B stars. Examination of the spectra does not reveal any stellar absorption lines, indicating that the contribution from starlight is negligible. We do not subtract the iron emission forest as this component is usually not strong around the C IV emission line (e.g., Shen et al. 2008), and the wavelength coverage of the *HST* and *IUE* spectra is frequently too narrow (only a few hundred Angstroms) to fit this component. The Balmer continuum “small blue bump” only appears in the wavelength range between 2000–4000 Å, so its contribution is negligible around the C IV region.

The emission-line spectrum is obtained after subtracting the power-law continuum. We fit the C IV emission lines using two Gaussian profiles. The model always produces visually acceptable fits. We mask narrow absorption-line features appearing near the emission-lines so as not to underpredict the emission line flux. The equivalent widths, the emission-line luminosities under the assumption of isotropy, and the continuum monochromatic luminosities at 2500 Å are calculated under our adopted cosmology and are tabulated in Table 2.

To first order, we use 2–10 keV luminosities tabulated in Table 1 of Jiang et al. (2006) to

⁷For data processing of Sample B, refer to GBS08.

estimate $l_\nu(2 \text{ keV})$ under the assumption that the X-ray continuum is a single power-law with photon index $\Gamma = 2$ from 2 keV to 10 keV (e.g., Page et al. 2005; Shemmer et al. 2005; Vignali et al. 2005), so that

$$l_\nu(2 \text{ keV}) = \frac{L(2\text{--}10 \text{ keV})}{\nu_2 \ln 5} \quad (1)$$

where $h\nu_2 = 2 \text{ keV}$ and h is Planck’s constant. To obtain the Fe K α emission-line flux, we further assume that the Fe K α emission line resembles a single Gaussian profile: $f_1(\nu) = A \cdot e^{-(\nu-\nu_0)^2/2\sigma^2}$. This allows one to express the line flux F_1 in terms of $l_\nu(2 \text{ keV})$ or $F(2\text{--}10 \text{ keV})$, the Fe K α equivalent width $\text{EW}(\text{Fe K}\alpha)$, and the central energy ($\epsilon_0 = 6.4 \text{ keV}$) of the emission line. Assuming the continuum flux $f_c = C \cdot \nu^{-1}$, we can derive

$$\text{EW}(\text{Fe K}\alpha) = \int_0^{+\infty} \frac{f_1(\nu)}{f_c(\nu)} d\nu = \frac{A}{C} \left[\sigma^2 e^{-\nu_0^2/2\sigma^2} + \nu_0 \left(\sqrt{2\pi}\sigma - \int_{\nu_0}^{+\infty} e^{-x^2/2\sigma^2} dx \right) \right] \approx \frac{A}{C} \sqrt{2\pi}\nu_0\sigma. \quad (2)$$

The Fe K α emission-line flux is

$$F_1 = \int_0^{+\infty} f_1(\nu) d\nu = A \left(\sqrt{2\pi}\sigma - \int_{\nu_0}^{+\infty} e^{-x^2/2\sigma^2} dx \right) \approx A\sqrt{2\pi}\sigma. \quad (3)$$

The approximations are valid because generally $\nu_0 \gg \sigma$ so $\nu_0^2/2\sigma^2 \gg 1$. For instance, $\epsilon_0(\text{Fe K}\alpha) = 6.4 \text{ keV}$ while the width, $\sigma(\text{Fe K}\alpha)$, is usually $\lesssim 0.1 \text{ keV}$; as a result, $e^{-\nu_0^2/2\sigma^2} \approx 0$. We can therefore calculate the Fe K α line flux by

$$F_1 = \frac{\text{EW}(\text{Fe K}\alpha)}{\epsilon_0} \frac{F(2\text{--}10 \text{ keV})}{\ln 5}. \quad (4)$$

The Fe K α EWs, emission-line luminosities, and 2 keV monochromatic luminosities of Sample A are tabulated in Table 3.

3.2.2. Sample B

For objects in Sample B, we directly adopt the fitting results from GBS08. In their paper, the SDSS spectral continua were fit with polynomials, and the C IV emission lines were fit with Voigt profiles. The different model in GBS08 from our work used to fit the C IV spectral region will not cause significant differences; because the continuum around C IV is not contaminated with other emission/absorption lines, the polynomial fit will produce almost the same result as the simple power-law fit. In addition, since both multiple Gaussian and Voigt profiles produce acceptable fits to the emission line, they will give nearly the same line flux. The X-ray spectral continua were fit using a broken power-law with the power-law break fixed at 2 keV in the rest-frame in order to obtain $l_\nu(2 \text{ keV})$.

3.2.3. Sample C

We fit the UV/optical spectra from the SDSS using a routine, described by Vanden Berk et al. (2009, in preparation), developed for SDSS quasar spectra. This routine fits the “underlying continuum” using three components simultaneously: a power-law, the iron emission forest, and the small blue bump. We adopt the UV iron emission template (1075–3090 Å) from Vestergaard & Wilkes (2001) and the optical template (3535–7534 Å) from Véron-Cetty, Joly & Véron (2004). We first make a preliminary estimate of the power-law component by connecting two “line-free” points in the spectra. This provides initial estimates of the power-law parameters for the subsequent comprehensive processing in which the spectra are fit by considering all three components mentioned above. We evaluate the fitting quality by calculating χ^2 values within some “line-free” windows. Finally, the continuum fit is subtracted from the original spectrum and the residuals are used to conduct emission-line fitting. For Sample C, the C IV emission-lines are fit by superpositions of two Gaussian profiles, which always yields acceptable fits for the data. We then calculate the C IV EW, emission-line luminosity, and monochromatic luminosity at 2500 Å (Table 2). We adopt the values of α_{ox} and 2 keV monochromatic luminosity from Just et al. (2007).

Examples of continuum and emission-line fits of the *HST*, *IUE* and SDSS spectra are presented in Fig. 2.

3.3. Error Analysis

In order to estimate the uncertainties in the measured quantities for objects in Samples A and C, we ran Monte Carlo simulations assuming a model with a perfect correlation between $\text{EW}(\text{C IV})$, $f(\text{C IV})$, and $f_{\nu}(2500 \text{ Å})$. For each spectrum, we add random noise to the original best fit to produce artificial spectra. The random noise follows a Gaussian distribution, and its amplitude is determined in one of two ways. For a spectrum from the *HST* or *IUE* database, we apply a low band pass filter, filtering out low-frequency signals via fast Fourier transformation.⁸ The residual signal is mostly noise. We then calculate the root-mean-square (RMS) of the noise and take this value as the random noise amplitude to be added onto the model spectrum. For a spectrum from the SDSS database, we simply use the uncertainty level associated with each pixel as the noise amplitude. For each spectrum, we produce 100 artificial spectra and fit them in exactly the same way as the observed spectrum. The error bar of a spectral parameter is then calculated as the RMS of 100 fitting results. The typical error bar shown in each plot (e.g., Fig. 3) is the median of all the error bars of points in that plot.

When evaluating the uncertainties of monochromatic luminosities, e.g., $l_{\nu}(2500 \text{ Å})$, we must consider the contribution from the error in the luminosity distances (important for the low-redshift

⁸<http://www.msi.umn.edu/software/idl/tutorial/idl-signal.html>

objects). To validate this, we calculate the ratio of luminosity uncertainties without considering distance errors (δ_f ; the error in the flux measurement) to luminosity uncertainties after considering distance errors ($\delta_{f,d}$) for objects in Sample A, and denote it as $\delta_f/\delta_{f,d}$, in which f stands for flux and d stands for distance. Assuming that the square of total uncertainty can be expressed as the quadratic summation of the uncertainties of flux and distance individually, the square of the ratio, $(\delta_f/\delta_{f,d})^2$, is more relevant than the ratio itself. We find that there are 5 out of 50 objects (in Sample A) whose ratios are above 0.1; three of them are even greater than 0.5. These objects have very low redshifts but large redshift uncertainties ($\delta_z > 0.001$). For consistency, it is necessary to include the distance into the gross uncertainty calculation for all the objects in our samples. These uncertainties are also estimated using a Monte Carlo method. We adopt the most accurate values of redshift and their uncertainties from the NASA/IPAC Extragalactic Database.⁹ These uncertainties are treated as noise amplitudes to be added to the redshift values. The luminosity uncertainties are calculated using the following error-propagation equation:

$$\delta L = 4\pi d_L \sqrt{(d_L \delta f)^2 + 4f^2 (\delta d_L)^2}$$

We adopt a 20% uncertainty for each X-ray continuum luminosity, e.g., $l_\nu(2 \text{ keV})$; their measurement errors are not available in the literature. The relative uncertainty varies considerably depending on the number of X-ray counts. For Sample A, when the Fe K α emission lines are detected, the total number of counts is at least ~ 500 . The Fe K α emission-line luminosity and flux errors are calculated using the maximum error estimates. For instance, the upper bound of $L(\text{Fe K}\alpha)$ is calculated using the upper bounds of both $\text{EW}(\text{Fe K}\alpha)$ and $L(2\text{--}10 \text{ keV})$; the upper bound of $f(\text{Fe K}\alpha)$ is calculated using the upper bound of $L(\text{Fe K}\alpha)$ and the lower bound of luminosity distance $d_L - \delta d_L$. This uncertainty ignores any systematic uncertainty produced by errors in the cosmological model.

For Sample B, because the parameter uncertainties are not given in GBS08, we simply apply a 20% uncertainty for all luminosity values as a first-order approximation.

4. Drivers of the C IV Baldwin Effect

4.1. Comparison with Previous Work

We will first examine some important relations to determine if our measurements are consistent with previous work. It has been argued that α_{ox} has no detectable redshift dependence (e.g., Strateva et al. 2005; Steffen et al. 2006; but see Kelly et al. 2007), so in this paper we neglect any redshift evolution of α_{ox} .

⁹<http://nedwww.ipac.caltech.edu/>

Fig. 3 displays the plot of $\text{EW}(\text{C IV})$ against $l_\nu(2500 \text{ \AA})$ for the combined sample, distinguished by luminosity. We use the monochromatic luminosity at 2500 \AA rather than the traditional BEff wavelength (1450 \AA) because our choice is more convenient to compare the BEff with the correlation between C IV and α_{ox} . The luminosities at these two wavelengths are well correlated. The quantity f_{1400}/f_{2500} is Gaussian distributed with a dispersion of $\sigma \sim 0.15$ (Fig. 3 in Gibson et al. 2009), so using $l_\nu(2500 \text{ \AA})$ instead of $l_\nu(1450 \text{ \AA})$ should only add a small dispersion to the data points but will not significantly affect the slope of the BEff. We fit the data points linearly in logarithmic space using the EM (Expectation-Maximization) method (Dempster, Laird & Rubin 1977; Table 4). It is clear that $\text{EW}(\text{C IV})$ decreases with $l_\nu(2500 \text{ \AA})$ (Fig. 3).

It has been reported that the slope of the BEff becomes steeper for high-luminosity quasars. For example, Dietrich et al. (2002) obtained a C IV BEff slope (-0.14 ± 0.02), which was shallower than the value reported in previous studies (-0.22 ± 0.05 , Green 1996; also see Osmer, Porter & Green 1994; Laor et al. 1995). Using only the $\text{EW}(\text{C IV})$ measurements for their high-luminosity subsample with $\lambda L_\lambda(1450 \text{ \AA}) \gtrsim 10^{44} \text{ erg s}^{-1}$, Dietrich et al. (2002) obtained a steeper slope of the BEff of -0.20 ± 0.03 for C IV. To investigate the slope change with luminosity, we fit our data points with $l_\nu(2500 \text{ \AA}) < 30.5$. We find that the slope of the low-luminosity sample is consistent with the slope of the entire sample within 1σ (Table 4). Therefore, although our dataset exhibits a suggestive *trend* which disagrees with Dietrich et al. (2002), we do not find significant changes of slope over luminosity.

The large scatter in the BEff could have several causes, including observational error, intrinsic variation of the BEff (Osmer & Shields 1999; Shields 2007 and references therein), luminosity dependence of the BEff slope, and the redshift dependence of the BEff. Vanden Berk et al. (2009, in preparation) found that the slope of the BEff does not change across redshift, but its scaling factor (or equivalently, the EW of a broad emission line at a fixed monochromatic luminosity) exhibits a significant change. Our BEff slope is an overall average across the redshift and luminosity range we covered; remember that there is a strong redshift-luminosity correlation in our sample.

We examined the $l_\nu(2500 \text{ \AA})$ - $l_\nu(2 \text{ keV})$ and $l_\nu(2500 \text{ \AA})$ - α_{ox} relations for both Sample A and the combined sample using survival analysis (ASURV, Lavalley, Isobe & Feigelson, 1992) if censored data are involved, and find that all the results are consistent with previous work. When we calculate the slope of the Fe K α BEff, we apply the Buckley-James method (Table 4, Buckley & James 1979; Lavalley, Isobe & Feigelson 1992) included in ASURV to perform linear regression because the $\text{EW}(\text{Fe K}\alpha)$ contains censored values. The slope of the Fe K α BEff of Sample A (-0.115 ± 0.062) is consistent with the result from the RQ sample (-0.102 ± 0.052) in Jiang et al. (2006).

4.2. The Effects of α_{ox} on the C IV and Fe K α BEffs

Fig. 4 shows the plot of EW(C IV) against α_{ox} for the combined sample; the regression result from the EM algorithm for the linear relation is

$$\log \text{EW}(\text{C IV}) = (1.035 \pm 0.075)\alpha_{\text{ox}} + (3.301 \pm 0.119) \quad (5)$$

and the Spearman correlation coefficient is 0.607 ($P_0 < 0.001$).¹⁰ Because α_{ox} is an indicator of the hardness of the SED which controls the ionization level of C IV surrounding the central engine, Fig. 4 demonstrates that as the ionizing flux becomes harder (α_{ox} increases), the C IV emission has a strong positive response to α_{ox} .

Both α_{ox} and $l_{\nu}(2500 \text{ \AA})$ are correlated with EW(C IV); which is a more fundamental driver? To investigate this issue, we applied PCA to EW(C IV), $l_{\nu}(2500 \text{ \AA})$, and α_{ox} using the combined sample, Sample A, and a reduced sample. Table 5 presents Pearson, Spearman, and Kendall’s correlation and partial-correlation coefficients (if available), along with significance levels for these three samples. We present the statistical results of Sample A for comparing the correlation results of C IV and Fe K α . Because the combined sample contains censored data for the α_{ox} values, we must use survival analysis to calculate the correlation coefficients. However, algorithms are not available for calculating *all* the correlation and partial-correlation coefficients for censored data. For example, the empty entries in Table 5 are due to the unavailability of corresponding algorithms. In order to compare the changes of correlation strength when the third parameter is controlled, we construct a reduced sample with the censored data removed, considering that this only excludes a small fraction ($\sim 6\%$) of the entire data set and should not affect the statistical properties of the sample. We can see that the C IV BEff is significantly weakened when α_{ox} is held fixed; the correlation coefficient drops from -0.580 to -0.224 (Spearman). On the other hand, the correlation coefficient between EW(C IV) and α_{ox} also drops significantly when $l_{\nu}(2500 \text{ \AA})$ is held fixed, from 0.615 to 0.332 . This implies that both α_{ox} and $l_{\nu}(2500 \text{ \AA})$ are driving the change of EW(C IV).

The Fe K α BEff plot (not shown) of our sample (Sample A) is very similar to the correlation shown of Fig. 4 in Jiang et al. (2006) except that our sample size is smaller. Fig. 5 shows EW(Fe K α) plotted against α_{ox} . The Spearman test gives a much weaker correlation coefficient (-0.230 with $P_0 = 0.111$) than that for C IV (-0.304 with $P_0 < 0.001$). In addition, simple χ^2 fitting produces a slope of 0.046 ± 0.154 , consistent with zero. The consistency between the correlation analysis and regression result provides strong evidence that EW(Fe K α) is not correlated with α_{ox} .

4.3. Effects of AGN Variability on BEff Relation Scatter

Because of the ubiquity of AGN variability, combined with the different times of the optical and X-ray observations, our values of α_{ox} do not reflect the spectral hardness at a specific time

¹⁰ P_0 is the confidence level of the null hypothesis. Therefore, the smaller P_0 is the more likely the correlation exists.

but are randomly distributed around their mean values. The deviation of α_{ox} from its mean value would be ~ 0.083 , assuming that the variation amplitudes are 30% for $l_\nu(2500 \text{ \AA})$ and 40% for $l_\nu(2 \text{ keV})$ (e.g., Strateva et al. 2005, GBS08).

To check how much of the scatter of our correlations could be attributed to variability, we performed two simple tests on our combined sample. We follow the method used in § 3.1 of GBS08 and introduce $\Delta \log \text{EW}$, which is the difference between the observed $\text{EW}(\text{C IV})$ and the EW calculated from linear regression (Eq. 7), i.e., $\Delta \log \text{EW} = \log \text{EW} - \log \text{EW}(l_\nu(2500 \text{ \AA}))$. We define μ and σ as the mean and dispersion of the distribution of $\Delta \log \text{EW}$. To calculate μ and σ , we maximize the likelihood function (Maccacaro et al. 1988):

$$L = \prod_i \frac{1}{\sqrt{2\pi (\sigma_i^2 + \sigma^2)}} \exp \left[-(\Delta \log \text{EW}_i - \mu)^2 / 2(\sigma_i^2 + \sigma^2) \right] \quad (6)$$

in which the subscript i represents each object and σ_i is the uncertainty of $\Delta \log \text{EW}$ associated with each $\Delta \log \text{EW}_i$. The maximization of L requires $\mu = 0.01$ and $\sigma = 0.23$.

Next, we estimate the potential scatter of $\Delta \log \text{EW}$ due to variability. We need to consider two terms: $\log \text{EW}$ and $\log \text{EW}(l_\nu(2500 \text{ \AA}))$. To first approximation, $\text{EW} \sim f_{\text{line}}/f_{\text{cont}}$ in which f_{line} is the emission-line flux and the f_{cont} is the continuum flux. The emission-line variability of six luminous quasars at $z = 2.2\text{--}3.2$ was recently reported by Kaspi et al. (2007). The mean fractional variation F_{var}^{11} is ≈ 0.096 by averaging the fractional variation of C IV $\lambda 1549$ of all six quasars. The C IV emission-line variability of a number of Seyfert galaxies has been studied, including Fairall 9 (Rodríguez-Pascual et al. 1997), NGC 5548 (Clavel et al. 1991), NGC 7469 (Wanders et al. 1997), NGC 3783 (Reichert et al. 1994), and 3C 390.3 (O’Brien et al. 1998). By averaging the fractional variations of Seyferts and quasars above, we obtain an *average* emission-line variation $\langle F_{\text{var}} \rangle = 0.130$. The typical variation of $l_\nu(2500 \text{ \AA})$ is $\sim 30\%$ (e.g., Strateva et al. 2005). Therefore, the scattering of $\log \text{EW}$ contributed from variability is *estimated* (assuming all independent variables are Gaussian distributed) as

$$\sigma(\Delta \log \text{EW}) = \frac{1}{\ln 10} \sqrt{\left(\frac{\delta f_{\text{line}}}{f_{\text{line}}} \right)^2 + \left(\frac{\delta f_{\text{cont}}}{f_{\text{cont}}} \right)^2 + a^2 \left[\frac{\delta l_\nu(2500 \text{ \AA})}{l_\nu(2500 \text{ \AA})} \right]^2} \approx 0.144.$$

In the calculation above, $a = 0.198$ (Eq. (7)). This exercise indicates that at least 60% of the scatter around the BEff in our sample can be attributed to AGN variability.

We performed a similar test for the $\alpha_{\text{ox}}\text{-EW}(\text{C IV})$ relation. Because the set of α_{ox} contains censored data, we can only use the reduced data set (258 objects). The maximization of L (Eq. 6) yields $\mu = 0.01$ and $\sigma = 0.22$. The potential dispersion of this relation assuming all scatter comes

¹¹ F_{var} is defined as the RMS of the intrinsic variability relative to the mean flux (Rodríguez-Pascual et al. 1997).

from variability is *estimated* (assuming Gaussian distributions) as

$$\sigma(\Delta \log \text{EW}) = \frac{1}{\ln 10} \sqrt{\left(\frac{\delta f_{\text{line}}}{f_{\text{line}}}\right)^2 + \left(\frac{\delta f_{\text{cont}}}{f_{\text{cont}}}\right)^2 + (0.3838a)^2 \left[\left(\frac{\delta l_{\nu}(2500 \text{ \AA})}{l_{\nu}(2500 \text{ \AA})}\right)^2 + \left(\frac{\delta l_{\nu}(2 \text{ keV})}{l_{\nu}(2 \text{ keV})}\right)^2\right]} \approx 0.163.$$

In the calculation above, $a = 1.035$ (Eq. 5). This indicates that variability produces at least 75% of the scatter around the α_{ox} -EW(C IV) relationship.

In summary, the above two tests demonstrate that a substantial fraction, if not the majority, of the scatter in the correlations above can be attributed to X-ray and UV/optical variability. It should be possible to make the correlations tighter if the UV/optical and X-ray data are observed simultaneously.

4.4. Regressions of EW and Luminosity

The BEff provides a potential avenue to infer the luminosity of a quasar from emission-line observations. Type Ia supernovae (SNe) are treated as classical standard candles (e.g., Phillips 1993; Burrows 2000), but only a few are observed beyond $z \sim 1.5$. If quasars, which are much easier to detect than SNe and can be observed to much a higher redshift, can be used as standard candles, they would be an important tool for cosmological studies. Soon after the discovery of the BEff, many investigations considered the possibility of treating emission-line EW as a luminosity indicator (e.g., Baldwin 1977b; Wampler 1980). Unfortunately, the C IV BEff usually has a large scatter (Osmer & Shields 1999; Shields 2007); given the small slope in the $\log \text{EW} - \log l_{\nu}$ plot (on the order of -0.2), the predicted luminosities are very inaccurate. It has also been shown that the C IV BEff is redshift dependent (Francis & Koratkar 1995; Vanden Berk et al. 2009, in preparation), making it a less valuable probe of cosmology.

Because we are focusing on the influence of α_{ox} at the moment, and will put the redshift factor aside, we will concentrate on the issue of whether the scatter can be reduced if we regress EW(C IV) with $l_{\nu}(2500 \text{ \AA})$ and/or α_{ox} , and if the prediction of luminosity can be made more accurate with this approach. The linear-regression results of EW(C IV) with α_{ox} are already shown in Eq.(5). Similar regressions from $l_{\nu}(2500 \text{ \AA})$ and both of $l_{\nu}(2500 \text{ \AA})$ and α_{ox} , using the fully parametric EM algorithm, are

$$\log \text{EW(C IV)} = (-0.198 \pm 0.015) \log l_{\nu}(2500 \text{ \AA}) + (7.764 \pm 0.461) \quad (7)$$

$$\log \text{EW(C IV)} = (-0.107 \pm 0.021) \log l_{\nu}(2500 \text{ \AA}) + (0.615 \pm 0.106) \alpha_{\text{ox}} + (5.944 \pm 0.536). \quad (8)$$

in which EW(C IV) is in \AA and $l_{\nu}(2500 \text{ \AA})$ is in $\text{erg s}^{-1} \text{ Hz}^{-1}$. The last regression was performed on the combined sample without the censored data (258 objects) because the EM algorithm in ASURV does not allow both independent variables to contain censored data points.

To evaluate the scatter, we subtract the predicted EW values calculated using the above equations from the observed values and compute the RMS values of the residuals. We see a slight

improvement of the RMS values, using α_{ox} and both $l_{\nu}(2500 \text{ \AA}) + \alpha_{\text{ox}}$ (Table 6). The last regression result (Eq.(8)) is consistent with Eq.(11) in GBS08, indicating that at least part of the scatter of the BEff is due to α_{ox} .

Next, we regress luminosity against EW(C IV) and/or α_{ox} , using the combined sample. The results are

$$\log l_{\nu}(2500 \text{ \AA}) = (-1.980 \pm 0.154) \log \text{EW(C IV)} + (34.076 \pm 0.256) \quad (9)$$

$$\log l_{\nu}(2500 \text{ \AA}) = (-0.852 \pm 0.168) \log \text{EW(C IV)} - (2.864 \pm 0.262)\alpha_{\text{ox}} + (27.668 \pm 0.635). \quad (10)$$

The last regression was performed on the censored-data-excluded sample. We then calculate the RMS values of the residuals after subtracting the predictions from the equations above (Table 6). The RMS value shrinks by 18% using EW(C IV) + α_{ox} , compared to using EW(C IV) alone. We use the standard F -test to check if the two sets of residuals have consistent variance. The testing gives an F -statistic of 1.48 with a significance 0.002, indicating that these two sets of residuals have significantly different variances and 18% is a statistically significant improvement. To use quasars as standard candles via the BEff, we should at least confine the luminosity within an uncertainty of 30%, or, equivalently, $\text{rms} < 0.1$. This cannot be achieved using our current dataset and controlled parameters.

5. Relation Between Fe K α and C IV

Fe K α is important in AGN studies because it is the strongest emission line appearing in the X-ray band. However, the strength of this emission line varies significantly from object to object, and the line is not detected in most X-ray observations of quasars. Given this lack of direct observational measurement, it would be useful to develop a way to predict the expected strength of the line empirically.

The EW(C IV) and EW(Fe K α) do not exhibit a significant correlation (Fig. 6) in Sample A; the correlation has a low Spearman rank-correlation coefficient (0.319 with $P_0 = 0.027$). Although the EWs of the two lines are not well correlated, their luminosities and fluxes are strongly correlated (Fig. 7), with Spearman correlation coefficients 0.529 ($P_0 < 0.001$) and 0.551 ($P_0 < 0.001$), respectively (Table 7). The linear correlations regressed in Fig. 7 are

$$\log L(\text{Fe K}\alpha) = (0.588 \pm 0.079) \log L(\text{C IV}) + (16.164 \pm 3.416) \quad (11)$$

$$\log f(\text{Fe K}\alpha) = (0.978 \pm 0.188) \log f(\text{C IV}) - (2.082 \pm 2.228). \quad (12)$$

One must always question the significance of relations such as (11) because even if there is no correlation between the observed fluxes of the lines, the fact that the line luminosities for a given object contain the same distance factor will introduce an apparent correlation in the luminosities. To investigate whether this effect is important for our study, we perform a test in which we conduct

correlation and regression analysis for a sub-sample of Sample A. Objects in this sub-sample have similar redshifts, and thus they have approximately the same distances. First, we use objects with $0.06 < z < 0.09$ because this redshift bin contains a large number of objects. This sub-sample contains 10 objects. The correlation coefficient of $f(\text{Fe K}\alpha)$ - $f(\text{C IV})$ is 0.624 ($P_0 = 0.061$) and of $L(\text{Fe K}\alpha)$ - $L(\text{C IV})$ is 0.709 ($P_0 = 0.033$). The regression results are

$$\log L(\text{Fe K}\alpha) = (0.748 \pm 0.200) \log L(\text{C IV}) + (9.330 \pm 8.702) \quad (13)$$

$$\log f(\text{Fe K}\alpha) = (0.771 \pm 0.241) \log f(\text{C IV}) - (4.280 \pm 2.819). \quad (14)$$

Both the correlation and regression results of this sub-sample are consistent with the results of the entire sample within uncertainties, suggesting that the luminosity correlation of the C IV and Fe K α lines may be real and is not a consequence of multiplying the two fluxes of a given object by the same large distance factor. The luminosity of C IV emission line increases faster than the luminosity of Fe K α .

One might be concerned that the correlation between $L(\text{Fe K}\alpha)$ and $L(\text{C IV})$ is *artificial* because the calculation of the Fe K α measurements involves $L(2\text{--}10 \text{ keV})$ (Eq. (4)), which is proportional to $l_\nu(2 \text{ keV})$ (Eq. (1)), and $l_\nu(2 \text{ keV})$ is correlated with $l_\nu(2500 \text{ \AA})$, which is correlated with $\text{EW}(\text{C IV})$, i.e., the C IV BEff. $\text{EW}(\text{C IV})$ is calculated from continuum and emission line luminosity, so apparently, the $L(\text{Fe K}\alpha)$ and $L(\text{C IV})$ are not independent before we perform the correlation. However, our calculation of Fe K α is simply reversing the $F(2\text{--}10 \text{ keV})/\text{EW}$ calculation of Jiang et al. (2006), so $F(\text{Fe K}\alpha)$ is not actually dependent of $F(2\text{--}10 \text{ keV})$ and hence $l_\nu(2500 \text{ \AA})$. In essence, we have the values of $F(\text{Fe K}\alpha)$ independent of $F(\text{C IV})$. Therefore, our $L(\text{Fe K}\alpha)$ and $L(\text{C IV})$ correlation, which is *expected* from existing relations, is not an artifact correlation.

That the EWs of C IV and Fe K α are uncorrelated is consistent with the result by Page et al. (2004) and further demonstrates that the C IV and Fe K α emission lines are unlikely to have the same origin. This result is not surprising because Fe K α and C IV are produced in different processes. The correlation between their luminosities is probably a combination of effects between their EWs (uncorrelated) and continuum (strongly correlated). The flux correlation, although empirical and not very tight, is a useful first order estimation of the Fe K α line flux given the UV spectra in the rest-frame of an AGN.

6. Discussions and Conclusions

We have compiled a sample of 272 Type 1 AGNs and quasars that have UV and X-ray measurements, among which Fe K α emission lines are detected in 50 objects. The sample covers a wide range of redshift ($0.009 \lesssim z \lesssim 4.720$), and a wide range of luminosity from Seyfert galaxies to the most-luminous quasars ($27.81 \lesssim \log l_\nu(2500 \text{ \AA}) \lesssim 33.04$). These properties allow us to study the overall properties of AGNs rather than focusing on a particular redshift or luminosity. It also has a high X-ray detection rate ($\sim 96\%$), which lets us obtain robust statistics. We have performed correlation and regression analyses using this sample and draw the following conclusions:

1. The C IV BEff is driven by both α_{ox} and $l_{\nu}(2500 \text{ \AA})$, or equivalently, by $l_{\nu}(2 \text{ keV})$ and $l_{\nu}(2500 \text{ \AA})$. This implies that changes in the ionizing flux induce changes in the ionization state of the BELR, producing more C IV ions when the SED becomes harder and vice versa. This is supported both by correlation and regression analyses:
 - The partial correlation between EW(C IV) and $l_{\nu}(2500 \text{ \AA})$ when α_{ox} is controlled is weaker than the regular correlation between EW(C IV) and $l_{\nu}(2500 \text{ \AA})$.
 - The scatter in the linear regression decreases when we regress EW with $\alpha_{\text{ox}} + l_{\nu}(2500 \text{ \AA})$ compared with $l_{\nu}(2500 \text{ \AA})$ alone.

Although the reduction of the scatter due to adding another regression parameter is not sufficiently large to treat quasars as standard candles, it demonstrates that a significant fraction of the scatter attributes to α_{ox} , and can be reduced by including it in regression analysis.

2. EW(Fe K α) exhibits no strong correlation with either α_{ox} or EW(C IV). This implies that Fe K α is not likely to have the same origin as C IV.
3. There may be a correlation between the luminosities of Fe K α and C IV with a logarithmic slope of 0.588 ± 0.079 . This correlation is possibly because both of these two quantities involve a factor related to the scale of the line emitting regions and the slope indicates that the C IV emission line luminosity increases faster than the Fe K α .

Although α_{ox} is a fundamental influence on EW(C IV), there is still a significant scatter in the EW(C IV)- α_{ox} diagram. As we have demonstrated, most of the scatter is contributed by variability, but another likely contribution source is the nature of α_{ox} which only connects the flux points at 2500 \AA and 2 keV but misses the Big Blue Bump, which is expected to play an important role in the photoionization process. The shape of an AGN SED can be very different depending on Eddington ratio ($L_{\text{bol}}/L_{\text{Edd}}$) but still have a fairly constant α_{ox} (Vasudevan & Fabian 2007). It is perhaps more appropriate to use a point near $\sim 250 \text{ \AA}$ instead of 2500 \AA to calculate a revised α_{ox} (Shemmer et al. 2008). This new α_{ox} might be more strongly correlated with EW(C IV). However, this requires challenging observations that cannot be achieved at present for most AGNs.

We thank Jane Charlton for providing a number of *HST*/FOS spectra of the core sample AGNs, Eric Feigelson for useful suggestions and advice on statistics, Ohad Shemmer and Dennis Just for discussions on linear regression, and Lanyu Mi for help with the statistical computations.

This work was partially supported by NSF grant AST-0607634 and NASA LTSA grant NAG5-13035.

Funding for the SDSS and SDSS-II has been provided by the Alfred P. Sloan Foundation, the Participating Institutions, the National Science Foundation, the U.S. Department of Energy, the National Aeronautics and Space Administration, the Japanese Monbukagakusho, the Max

Planck Society, and the Higher Education Funding Council for England. The SDSS website is <http://www.sdss.org/>.

REFERENCES

- Akritas, M. G., & Siebert, J. 1996, MNRAS, 278, 919
- Anderson, S. F., & Margon, B. 1987, ApJ, 314, 111
- Antonucci, R. 1993, ARA&A, 31, 473
- Avni, Y., & Tananbaum, H. 1982, ApJ, 262, L17
- Avni, Y., & Tananbaum, H. 1986, ApJ, 305, 83
- Bachev, R., Marziani, P., Sulentic, J. W., Zamanov, R., Calvani, M., & Dultzin-Hacyan, D. 2004, ApJ, 617, 171
- Baldwin, J. A. 1977a, ApJ, 214, 679
- Baldwin, J. A. 1977b, ApJ, 214, 679
- Baskin, A., & Laor, A. 2004, MNRAS, 350, L31
- Bianchi, S., Guainazzi, M., Matt, G., & Fonseca Bonilla, N. 2007, A&A, 467, L19
- Brandt, W. N., Laor, A., & Wills, B. J. 2000, ApJ, 528, 637
- Brinkmann, W. Laurent-Muehleisen, S. A., Voges, W., Siebert, J., Becker, R. H., Brotherton, M. S., White, R. L., & Gregg, M. D. 2000, A&A, 356, 445
- Buckley, J., & James, I. 1979, Biometrika, 66:429
- Burrows, A. 2000, Nature, 403, 727
- Carswell, R. F., & Smith, M. G. 1978, MNRAS, 185, 381
- Clavel, J., et al. 1991, ApJ, 366, 64
- Collinge, M. J., et al. 2001, ApJ, 557, 2
- Crenshaw, D. M., Kraemer, S. B., Boggess, A., Maran, S. P., Mushotzky, R. F., & Wu, C.-C. 1999, ApJ, 516, 750
- Crenshaw, D. M., & Kraemer, S. B. 2001, ApJ, 562, L29
- Croom, S. M., et al. 2002, MNRAS, 337, 275

- Dempster, A. P., Laird, N. M., & Rubin, D. B. 1977, *Royal Stat. Soc. B*, 39, 1
- Dietrich, M., Hamann, F., Shields, J. C., Constantin, A., Vestergaard, M., Chaffee, F., Foltz, C. B., & Junkkarinen, V. T. 2002, *ApJ*, 581, 912
- Fitzpatrick, E. L. 1999, *PASP*, 111, 63
- Francis, P. J., & Koratkar, A. 1995, *MNRAS*, 274, 504
- Gallagher, S. C., Brandt, W. N., Chartas, G., Priddey, R., Garmire, G. P., & Sambruna, R. M. 2006, *ApJ*, 644, 709
- Gibson, R. R., Brandt, W. N., & Schneider, D. P. 2008, *ApJ*, 685, 773 (GBS08)
- Gibson, R. R., et al. 2009, *ApJ*, 692, 758
- Green, P. J. 1996, *ApJ*, 467, 61
- Green, P. J. 1998, *ApJ*, 498, 170
- Green, P. J., Forster, K., & Kuraszkiewicz, J. 2001, *ApJ*, 556, 727
- Iwasawa, K., & Taniguchi, Y. 1993, *ApJ*, 413, L15
- Jiang, P., Wang, J. X., & Wang, T. G. 2006, *ApJ*, 644, 725
- Just, D. W., Brandt, W. N., Shemmer, O., Steffen, A. T., Schneider, D. P., Chartas, G., & Garmire, G. P. 2007, *ApJ*, 665, 1004
- Kaspi, S., Brandt, W. N., Maoz, D., Netzer, H., Schneider, D. P., & Shemmer, O. 2007, *ApJ*, 659, 997
- Kelly, B. C., Bechtold, J., Siemiginowska, A., Aldcroft, T., & Sobolewska, M. 2007, *ApJ*, 657, 116
- Kendall, M. G. 1938, *Biometrika*, 30, 18
- Kendall, M. G. 1970, *Rank Correlation Methods* (4th ed.; New York: Hafner)
- Kinney, A. L., Rivolo, A. R., & Koratkar, A. P. 1990, *ApJ*, 357, 338
- Korista, K., Baldwin, J., & Ferland, G. 1998, *ApJ*, 507, 24
- Krolik, J. H., Madau, P., & Zycki, P. T. 1994, *ApJ*, 420, L57
- Laor, A., Bahcall, J. N., Jannuzi, B. T., Schneider, D. P., & Green, R. F. 1995, *ApJS*, 99, 1
- Lavalley, M., Isobe, T., & Feigelson, E. 1992, *Astronomical Data Analysis Software and Systems I*, 25, 245
- Maccacaro, T., Gioia, I. M., Wolter, A., Zamorani, G., & Stocke, J. T. 1988, *ApJ*, 326, 680

- McDowell, J. C., Canizares, C., Elvis, M., Lawrence, A., Markoff, S., Mathur, S., & Wilkes, B. J. 1995, *ApJ*, 450, 585
- Nandra, K., George, I. M., Mushotzky, R. F., Turner, T. J., & Yaqoob, T. 1997, *ApJ*, 488, L91
- Netzer, H., Laor, A., & Gondhalekar, P. M. 1992, *MNRAS*, 254, 15
- O’Brien, P. T., et al. 1998, *ApJ*, 509, 163
- Osmer, P. S., Porter, A. C., & Green, R. F. 1994, *ApJ*, 436, 678
- Osmer, P. S., & Shields, J. C. 1999, *Quasars and Cosmology*, 162, 235
- Osterbrock, D. E. 1981, *ApJ*, 249, 462
- Osterbrock, D. E. 1989, *Astrophysics of Gaseous Nebulae and Active Galactic Nuclei* (Mill Valley: University Science Books)
- Page, K. L., O’Brien, P. T., Reeves, J. N., & Turner, M. J. L. 2004, *MNRAS*, 347, 316
- Page, K. L., Reeves, J. N., O’Brien, P. T., & Turner, M. J. L. 2005, *MNRAS*, 364, 195
- Peterson, B. M., et al. 2004, *ApJ*, 613, 682
- Phillips, M. M. 1993, *ApJ*, 413, L105
- Reichert, G. A., et al. 1994, *ApJ*, 425, 582
- Rodriguez-Pascual, P. M., et al. 1997, *ApJS*, 110, 9
- Schlegel, D. J., Finkbeiner, D. P., & Davis, M. 1998, *ApJ*, 500, 525
- Schneider, D. P., et al. 2005, *AJ*, 130, 367
- Schneider, D. P., et al. 2007, *AJ*, 134, 102
- Shang, Z., Wills, B. J., Wills, D., & Brotherton, M. S. 2007, *AJ*, 134, 294
- Shemmer, O., Brandt, W. N., Vignali, C., Schneider, D. P., Fan, X., Richards, G. T., & Strauss, M. A. 2005, *ApJ*, 630, 729
- Shemmer, O., et al. 2006, *ApJ*, 644, 86
- Shemmer, O., Brandt, W. N., Netzer, H., Maiolino, R., & Kaspi, S. 2008, *ApJ*, 682, 81
- Shen, Y., Greene, J. E., Strauss, M. A., Richards, G. T., & Schneider, D. P. 2008, *ApJ*, 680, 169
- Shields, J. C. 2007, *Astronomical Society of the Pacific Conference Series*, 373, 355

- Steffen, A. T., Strateva, I., Brandt, W. N., Alexander, D. M., Koekemoer, A. M., Lehmer, B. D., Schneider, D. P., & Vignali, C. 2006, *AJ*, 131, 2826
- Stoughton, C., et al. 2002, *AJ*, 123, 485
- Strateva, I. V., Brandt, W. N., Schneider, D. P., Vanden Berk, D. G., & Vignali, C. 2005, *AJ*, 130, 387
- Tananbaum, H., et al. 1979, *ApJ*, 234, L9
- Tanaka, Y., Inoue, H., & Holt, S. S. 1994, *PASJ*, 46, L37
- Vanden Berk, D. E., et al. 2001, *AJ*, 122, 549
- Vanden Berk, D. et al. 2009, in preparation
- Vasudevan, R. V., & Fabian, A. C. 2007, *MNRAS*, 381, 1235
- Véron-Cetty, M.-P., Joly, M., & Véron, P. 2004, *A&A*, 417, 515
- Vestergaard, M., & Wilkes, B. J. 2001, *ApJS*, 134, 1
- Vignali, C., Brandt, W. N., & Schneider, D. P. 2003, *AJ*, 125, 433
- Vignali, C., Brandt, W. N., Schneider, D. P., & Kaspi, S. 2005, *AJ*, 129, 2519
- Wampler, E. J. 1980, *Objects of High Redshift*, 92, 119
- Wandel, A., Peterson, B. M., & Malkan, M. A. 1999, *ApJ*, 526, 579
- Wanders, I., et al. 1997, *ApJS*, 113, 69
- Warner, C., Hamann, F., & Dietrich, M. 2004, *ApJ*, 608, 136
- Weaver, K. A., et al. 1992, *ApJ*, 401, L11
- Wilkes, B. J., Tananbaum, H., Worrall, D. M., Avni, Y., Oey, M. S., & Flanagan, J. 1994, *ApJS*, 92, 53
- Wise, J. H., Eracleous, M., Charlton, J. C., & Ganguly, R. 2004, *ApJ*, 613, 129
- York, D. G., et al. 2000, *AJ*, 120, 1579
- Zamorani, G., et al. 1981, *ApJ*, 245, 357
- Zamorani, G., Marano, B., Mignoli, M., Zitelli, V., & Boyle, B. J. 1992, *MNRAS*, 256, 238
- Zheng, W., & Malkan, M. A. 1993, *ApJ*, 415, 517
- Zhou, X.-L., & Wang, J.-M. 2005, *ApJ*, 618, L83

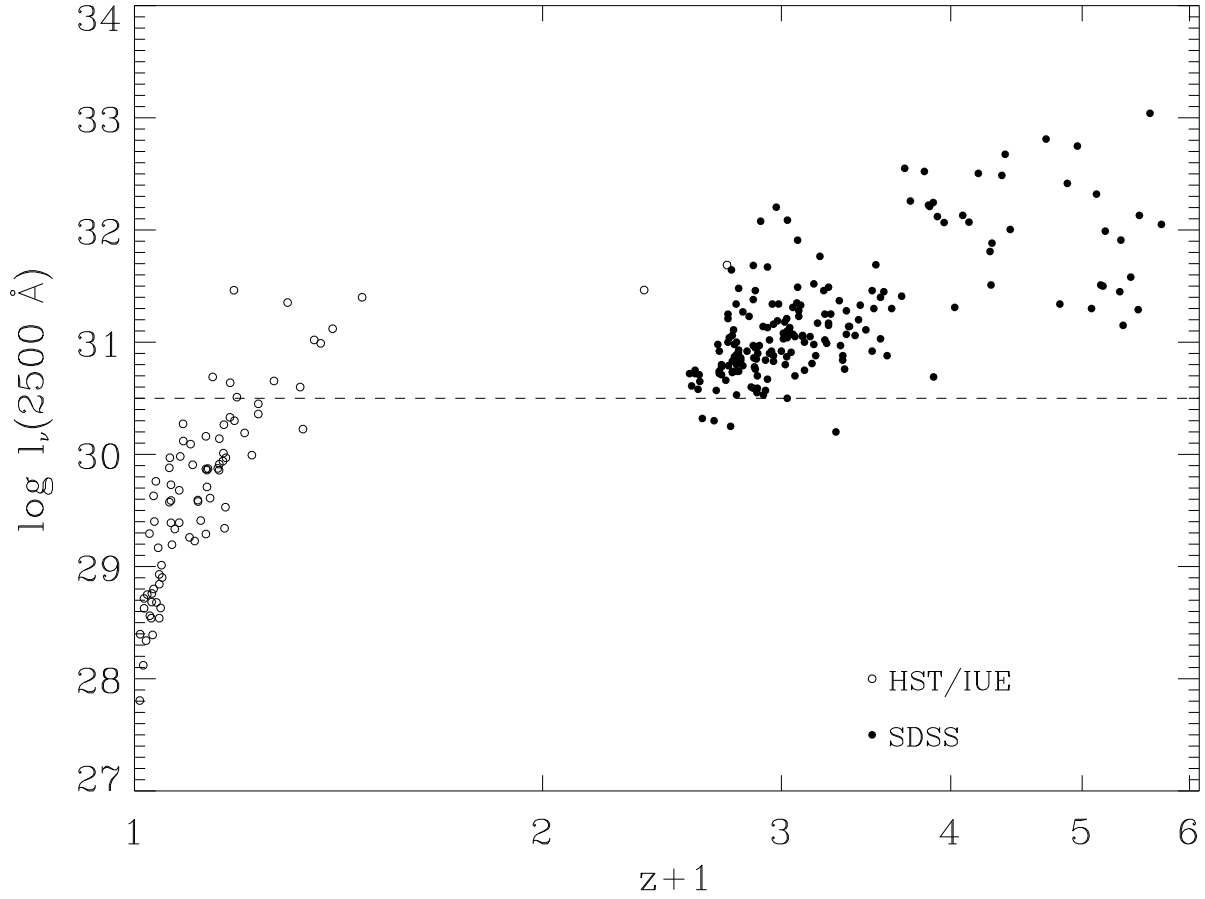


Fig. 1.— The luminosity-redshift diagram of the combined sample containing 272 objects distinguished by observational facilities. The gap for $0.5 \lesssim z \lesssim 1.5$ arises because of the detection limit of *HST/IUE* and wavelength coverage of the SDSS. The dashed line marks the position where $l_\nu(2500 \text{ \AA}) = 30.5$.

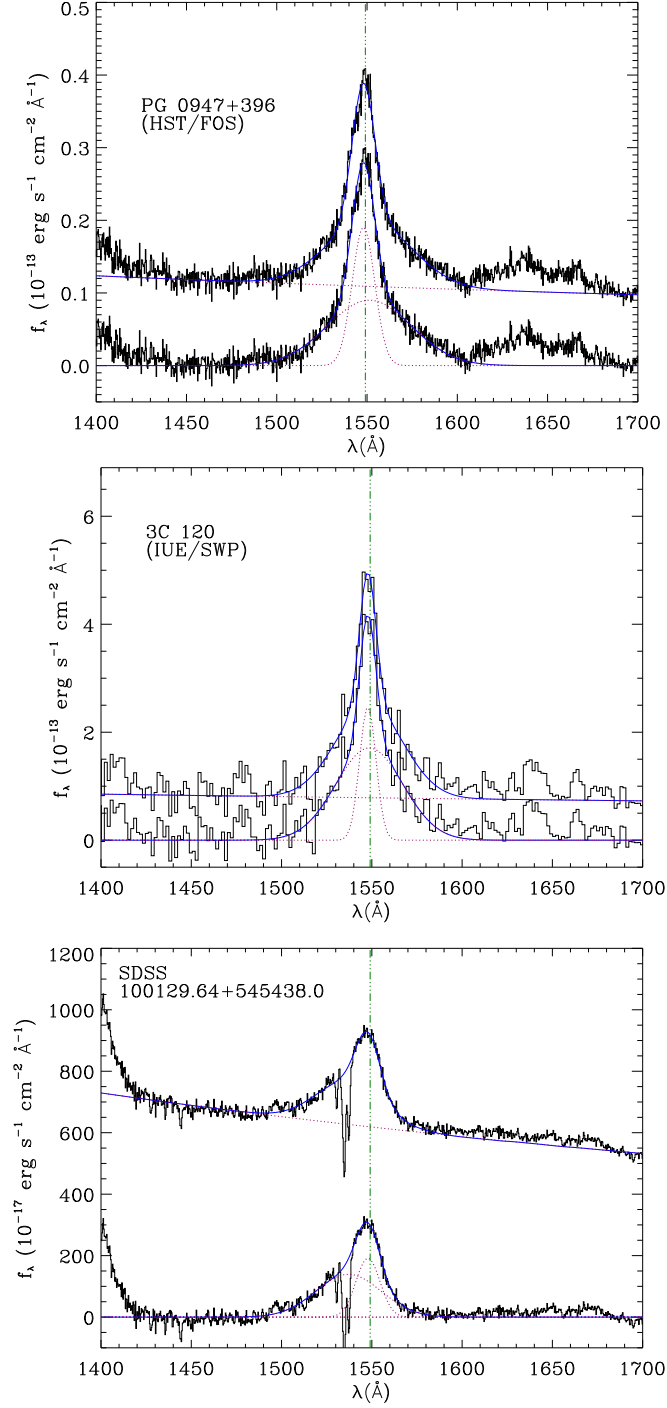


Fig. 2.— Continuum and C IV emission-line fit examples. In each panel, the upper spectrum is the original and the lower spectrum is continuum subtracted; blue solid curves are the fits to the spectra. The cyan dotted curves are emission-line components. For PG 0947+396 and 3C 120, these components include the power-law continua and two Gaussian profiles for C IV. For SDSS J100129.64+545438.0, we also plot the iron emission forest and small Balmer bump components, although they are so weak that they are almost invisible. The rest-frame spectral resolutions of these spectra are, from top to bottom, ~ 1.6 Å, ~ 5 Å, ~ 0.8 Å.

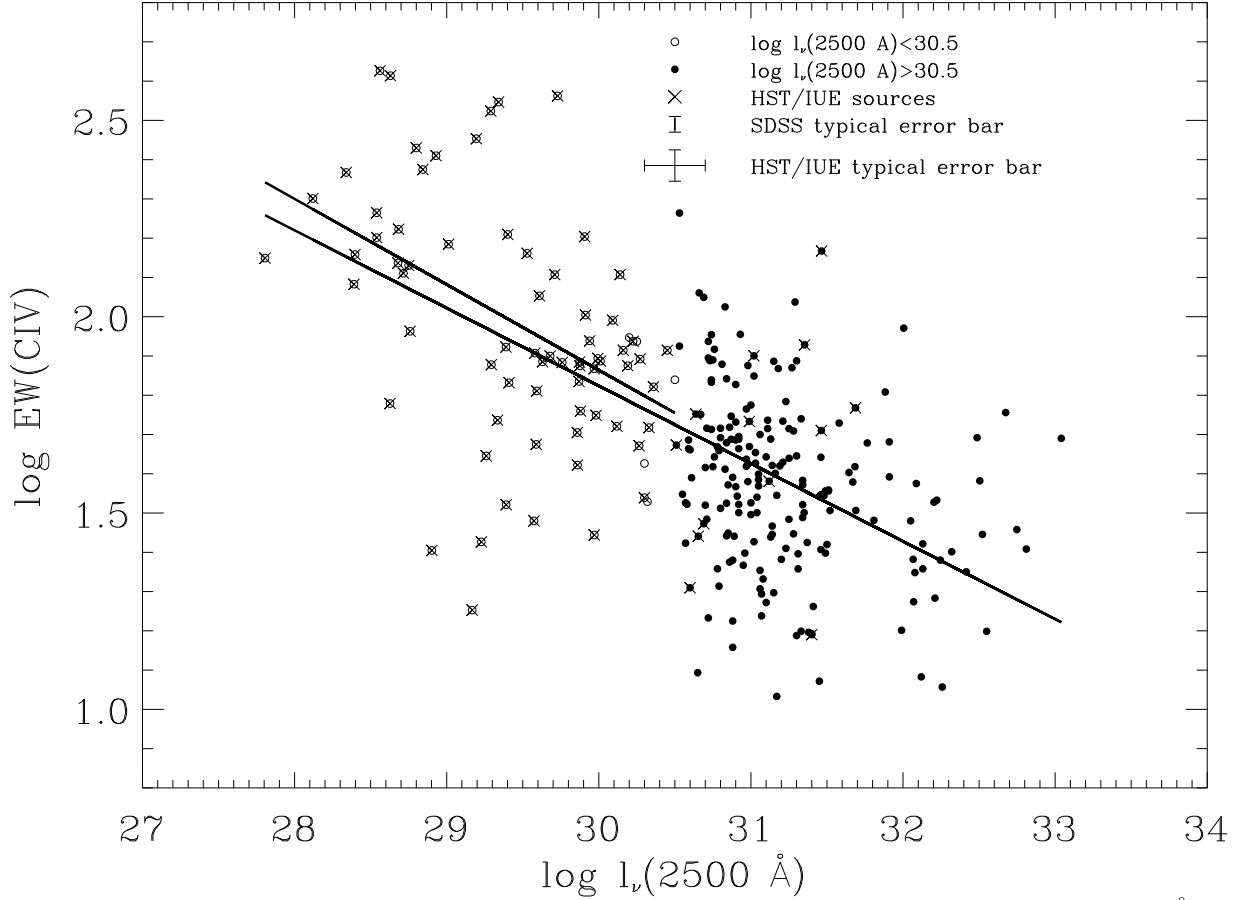


Fig. 3.— The C IV BEff diagram for the combined sample. The $\text{EW}(\text{C IV})$ is given in Å, and $l_\nu(2500 \text{ Å})$ is in units of $\text{erg s}^{-1} \text{Hz}^{-1}$. Points are distinguished by luminosity; the short solid line is the best linear fit to low-luminosity points and the long one is the best linear fit to the entire sample.

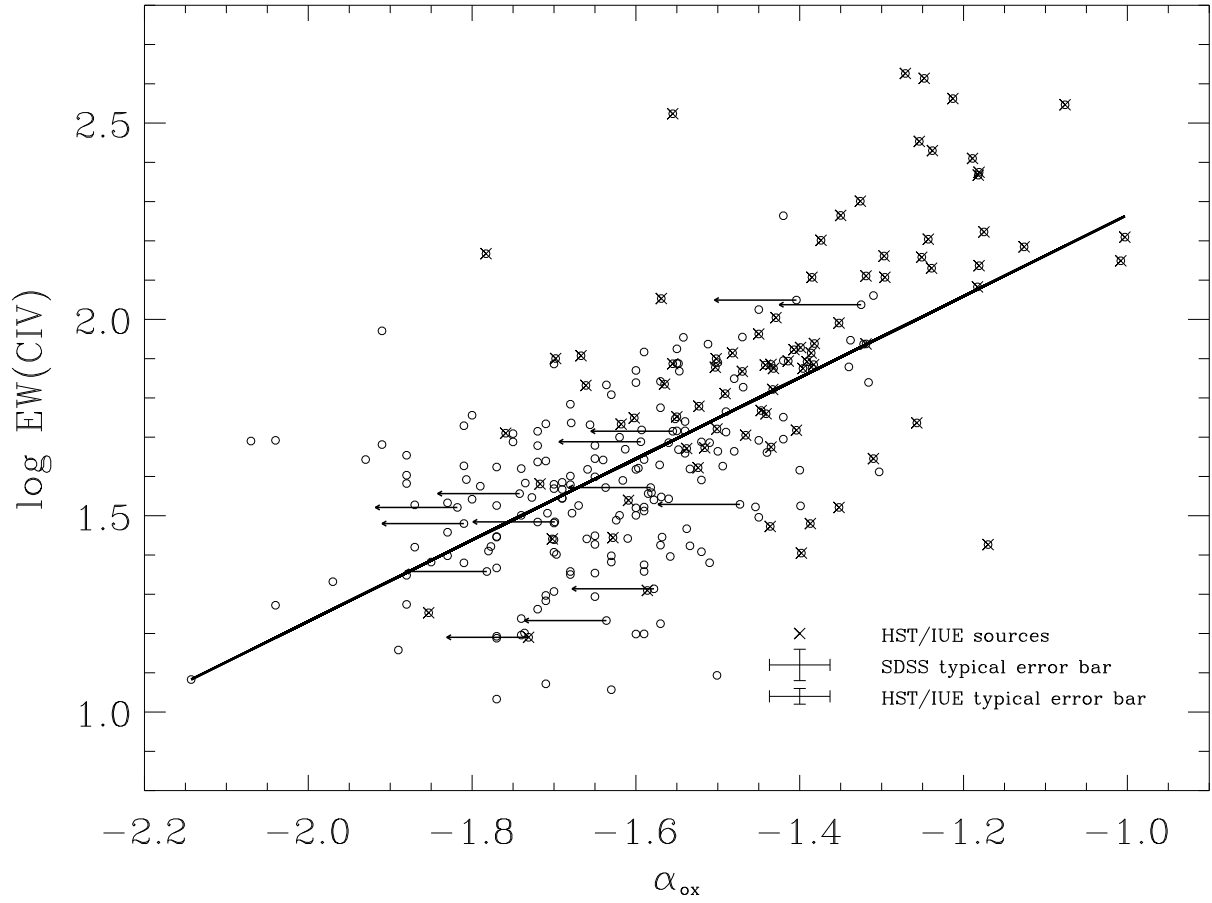


Fig. 4.— The correlation between $\text{EW}(\text{C IV})$ and α_{ox} . Upper limits on α_{ox} are marked with arrows. The solid line is the best linear fit using the EM algorithm.

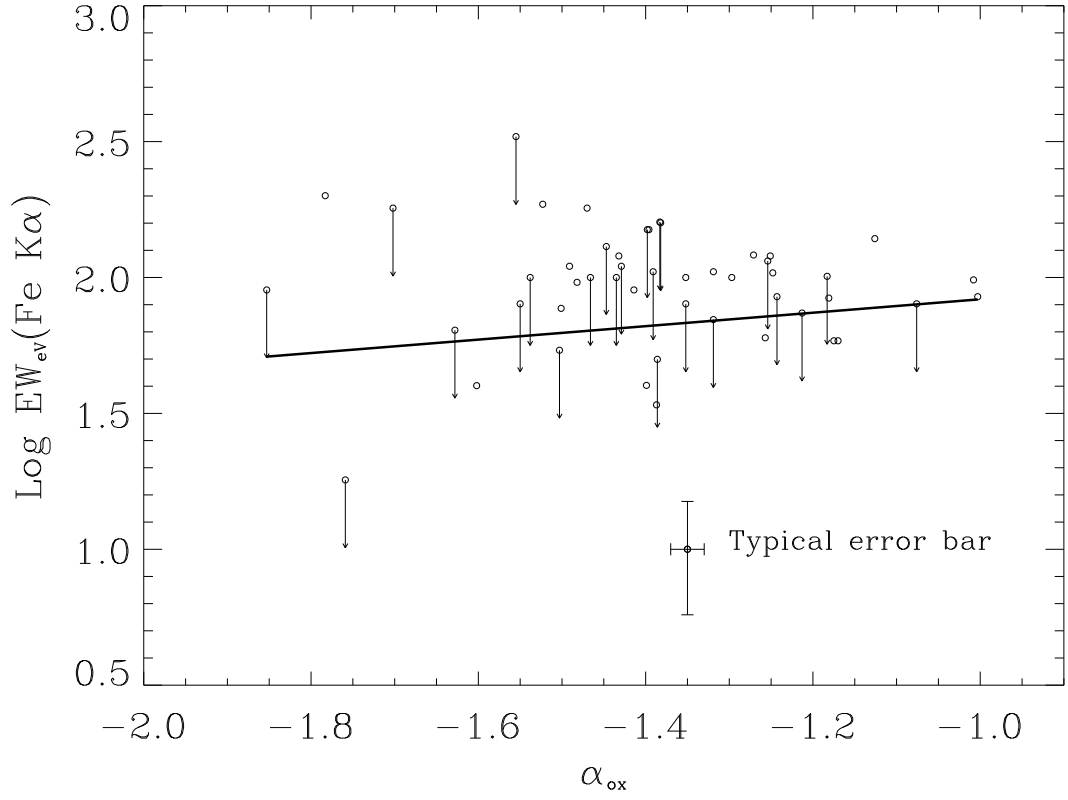


Fig. 5.— The correlation between $\text{EW}(\text{Fe } K\alpha)$ and α_{ox} for the core sample. The solid line is a linear fit using the ASURV package for the censored data. The typical error bar of the data is displayed at the top-right corner of the plot.

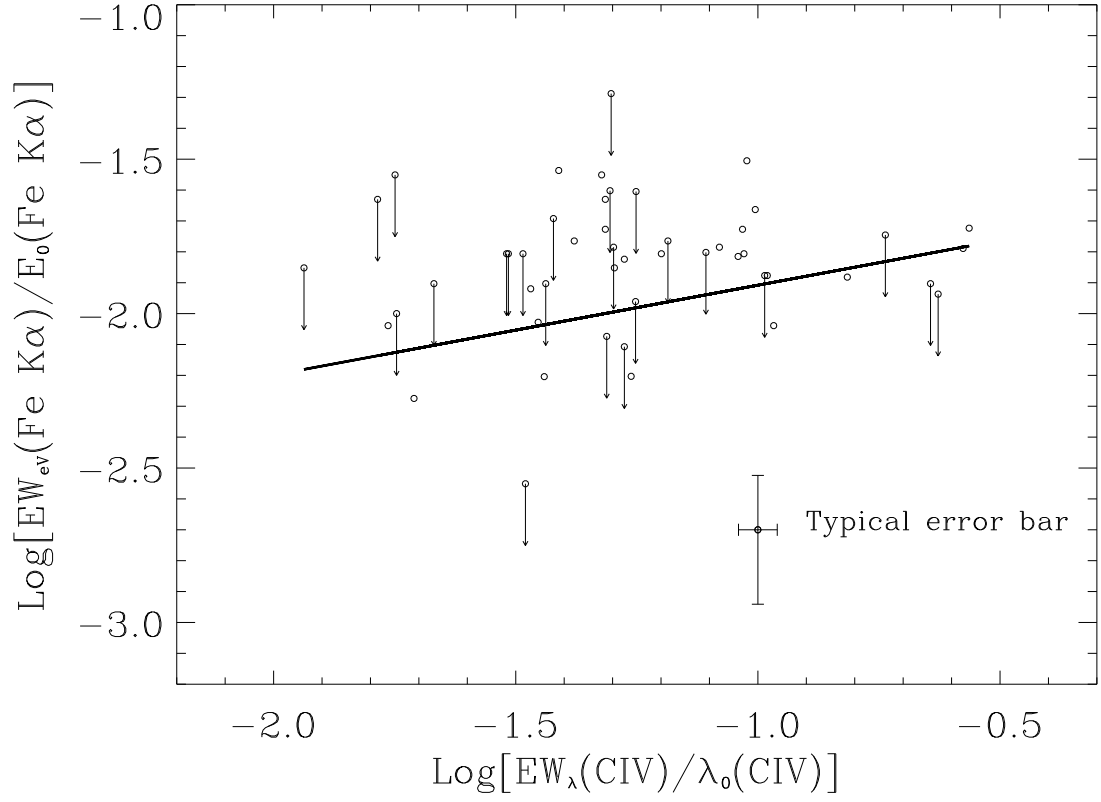


Fig. 6.— Plot of $\log [\text{EW}(\text{Fe K}\alpha)/E_0(\text{Fe K}\alpha)]$ vs. $\log [\text{EW}(\text{C IV})/\lambda_0(\text{C IV})]$ for the core sample. Because the units of $\text{EW}(\text{Fe K}\alpha)$ and $\text{EW}(\text{C IV})$ are different, we divide them by central energy $E_0(\text{Fe K}\alpha) = 6.4 \text{ keV}$ and central wavelength $\lambda_0(\text{C IV})$ to make them dimensionless.

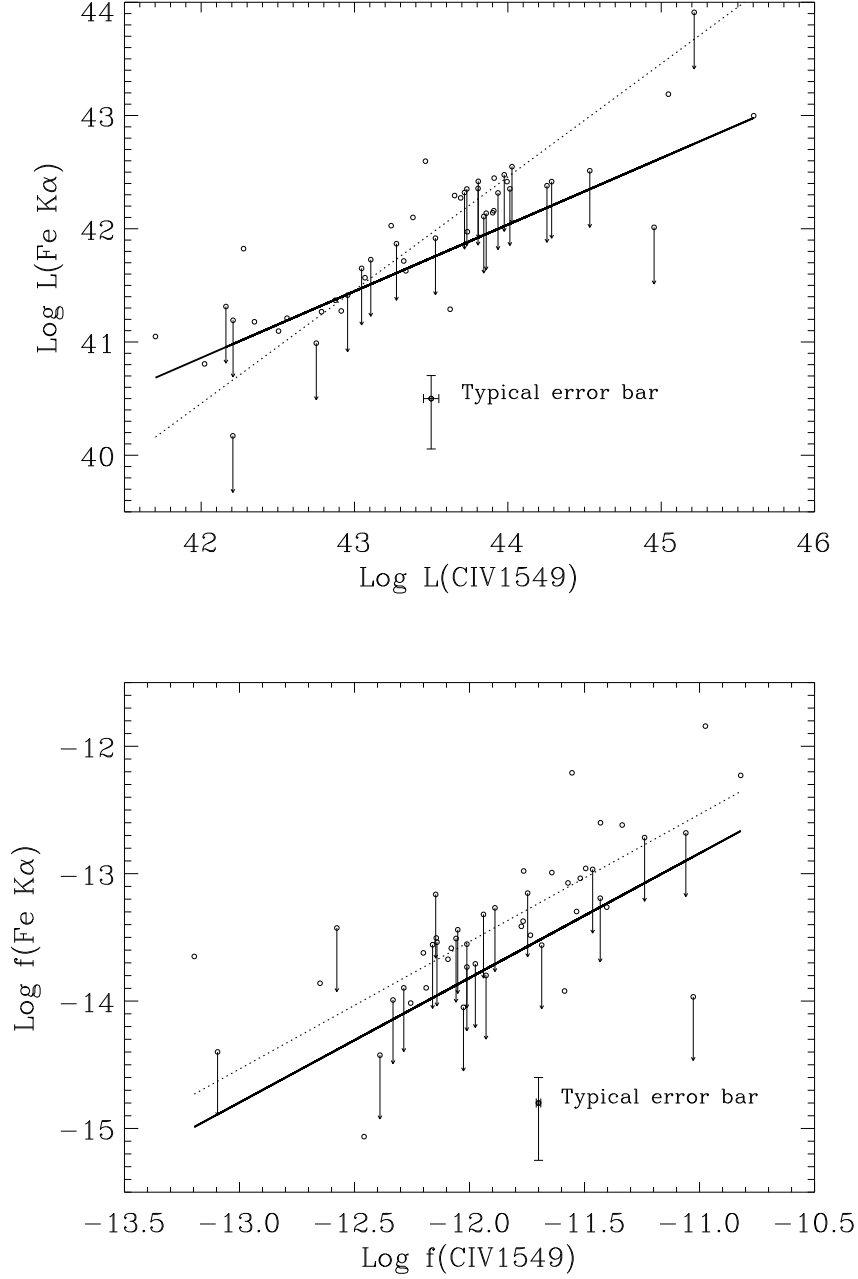


Fig. 7.— Plot of $\log L(\text{Fe K}\alpha)$ vs. $\log L(\text{C IV})$ (upper panel) and $\log f(\text{Fe K}\alpha)$ vs. $\log f(\text{C IV})$ (lower panel) for the core sample. Upper limits are denoted as downward arrows. The solid lines are the best linear fits to the data using ASURV. For comparison, we show the best linear fits with a unity slope in dotted lines. The data symbols and typical error bars are labelled at the bottom right corners.

Table 1. Summary of samples.

Sample	SDSS	HST	IUE	Total	Redshift range	$\log l_\nu(2500 \text{ \AA})$ range
A	0	34	16	50	0.009–1.735	27.81–31.69
B	98	0	0	98	1.7–2.7	30.53–31.67
C	91	13	20	124	0.015–4.720	28.12–33.04
Combined	189	47	36	272	0.009–4.720	27.81–33.04

Table 2. UV properties of the combined sample.

Object	z	$\log l_\nu(2500 \text{ \AA})$ ($\text{erg s}^{-1} \text{ Hz}^{-1}$)	EW(C iv) (\AA)	α_{ox}	Flag ¹	UV/Optical Instrument	Sample
NGC4593	0.009	27.81 ± 0.15	141.0 ± 23.2	-1.008 ± 0.066	0	HST	A
NGC3783	0.010	28.40 ± 0.08	144.0 ± 9.4	-1.251 ± 0.045	0	HST	A
Mkn352	0.015	28.12 ± 0.15	200.0 ± 12.9	-1.326 ± 0.067	0	IUE	C
Mrk1044	0.016	28.63 ± 0.04	60.1 ± 1.3	-1.523 ± 0.037	0	HST	A
NGC7469	0.016	28.72 ± 0.28	129.0 ± 25.1	-1.319 ± 0.111	0	HST	A
MCG8–11-11	0.020	28.34 ± 0.19	233.0 ± 39.1	-1.182 ± 0.082	0	IUE	C
Mkn79	0.022	28.75 ± 0.09	135.0 ± 11.3	-1.239 ± 0.049	0	IUE	C
Mrk335	0.026	29.29 ± 0.18	75.5 ± 7.7	-1.503 ± 0.077	0	HST	A

Note. — Table 2 is published in its entirety in the electronic version of the *Astrophysical Journal*. The portion is shown here for guidance regarding its form and content.

¹A value of “1” indicates that α_{ox} for this object is an upper limit.

Table 3. UV and X-ray properties of Sample A objects.

Object	z	EW(Fe K α) (eV)	$\log l_\nu(2 \text{ keV})$ ($\text{erg s}^{-1} \text{ Hz}^{-1}$)	$\log L(\text{Fe K}\alpha)$ (erg s^{-1})	$\log f(\text{Fe K}\alpha)$ ($\text{erg s}^{-1} \text{ cm}^{-2}$)	$\log L(\text{Civ})$ (erg s^{-1})	$\log f(\text{Civ})$ ($\text{erg s}^{-1} \text{ cm}^{-2}$)
NGC4593	0.009	$98.0^{+21.0}_{-21.0}$	25.18 ± 0.09	$41.05^{+0.09}_{-0.10}$	$-12.21^{+0.08}_{-0.11}$	41.70 ± 0.03	-11.55 ± 0.03
NGC3783	0.010	$120.0^{+14.0}_{-14.0}$	25.14 ± 0.09	$41.10^{+0.05}_{-0.05}$	$-12.98^{+0.12}_{-0.17}$	42.50 ± 0.01	-10.82 ± 0.01
NGC7469	0.016	$105.0^{+25.0}_{-25.0}$	25.28 ± 0.09	$41.18^{+0.09}_{-0.12}$	$\lesssim -13.19$	42.35 ± 0.03	-11.43 ± 0.03
Mrk1044	0.016	$186.0^{+61.0}_{-61.0}$	24.66 ± 0.09	$40.81^{+0.12}_{-0.17}$	$-11.84^{+0.22}_{-0.48}$	42.02 ± 0.01	-11.76 ± 0.01
Mrk335	0.026	$\lesssim 54.0$	25.38 ± 0.09	$\lesssim 40.99$	$\lesssim -14.42$	42.75 ± 0.02	-11.43 ± 0.02
Mrk590	0.026	$121.0^{+65.0}_{-51.4}$	25.25 ± 0.09	$41.21^{+0.19}_{-0.24}$	$-13.41^{+0.17}_{-0.28}$	42.56 ± 0.01	-11.64 ± 0.01
Mrk290	0.030	$58.5^{+56.5}_{-43.4}$	25.62 ± 0.09	$41.27^{+0.29}_{-0.59}$	$-12.62^{+0.08}_{-0.09}$	42.79 ± 0.01	-11.52 ± 0.01
Mrk493	0.031	$\lesssim 101.0$	25.31 ± 0.09	$\lesssim 41.19$	$\lesssim -13.55$	42.21 ± 0.03	-12.15 ± 0.03

Note. — Table 3 is published in its entirety in the electronic version of the *Astrophysical Journal*. The portion is shown here for guidance regarding its form and content.

Table 4. Hypothesis and linear fitting results.

Fig	Sample	x	y	$\rho^1 (P_0^2)$	k^3
3	Combined	$\log l_\lambda(2500 \text{ \AA})$	$\log \text{EW}_\lambda(\text{C iv})$	$-0.559(< 0.001)$	-0.198 ± 0.015
3	Combined with $\log l_\nu(2500 \text{ \AA}) < 30.5$	$\log l_\lambda(2500 \text{ \AA})$	$\log \text{EW}_\lambda(\text{C iv})$	$-0.465(< 0.001)$	-0.218 ± 0.048
4	Combined	α_{ox}	$\log \text{EW}_\lambda(\text{C iv})$	$0.755(< 0.001)$	1.035 ± 0.075
5	Sample A	α_{ox}	$\log \text{EW}_{\text{eV}}(\text{Fe K}\alpha)$	$0.104(0.470)$	0.247 ± 0.230^4

¹Spearman rank correlation coefficient.

²Significance levels of Spearman’s rank correlation.

³Slope from EM algorithm.

⁴Calculated for Sample A using the Buckley-James method in the ASURV software package (Lavalley, Isobe & Feigelson 1992).

Table 5. Correlation and partial-correlation analysis results.

x	y	z^a	Spearman	Pearson	Kendall
Combined sample (279)					
log EW(C IV)	log l_ν (2500 Å)	α_{ox}	-0.237^b
log EW(C IV)	log l_ν (2500 Å)		$-0.599(<0.001)$...	$-0.400(<0.001)$
α_{ox}	log EW(C IV)	log l_ν (2500 Å)	0.260
α_{ox}	log EW(C IV)		$0.607(<0.001)$
Combined Sample Without Censored Data (258)					
log EW(C IV)	log l_ν (2500 Å)	α_{ox}	-0.224	-0.311	-0.220
log EW(C IV)	log l_ν (2500 Å)		$-0.580(<0.001)$	-0.605	$-0.417(<0.001)$
α_{ox}	log EW(C IV)	log l_ν (2500 Å)	0.332	0.258	0.284
α_{ox}	log EW(C IV)		$0.615(<0.001)$	0.587	0.450
Sample A (49)					
log EW(C IV)	log l_ν (2500 Å)	α_{ox}	0.120(0.291)	0.074(0.214)	0.036
log EW(C IV)	log l_ν (2500 Å)		$-0.304(0.001)$	$-0.304(0.001)$	$-0.180(0.001)$
log EW(Fe K α)	log l_ν (2 keV)	α_{ox}	<0.001
log EW(Fe K α)	log l_ν (2 keV)		$-0.230(0.111)$
α_{ox}	log EW(Fe K α)	log l_ν (2 keV)	-0.130
α_{ox}	log EW(Fe K α)		$0.104(0.470)$

Note. — The number in the parentheses after a correlation coefficient is its significance level. Because we are considering the null hypothesis, a small number indicates a possibility of a strong correlation.

^a z is the controlled parameter. If a z entry is not empty, we calculate the partial correlation of x and y while controlling for z ; otherwise, we only calculate the correlation of x and y .

^b For the Kendall's partial τ correlation coefficients, generally, the sampling distribution is unknown; therefore, the probability values are not available (Kendall 1938, 1970).

^{c,d} Because EW(Fe K α) is a set of censored data, we have to use a generalized correlation statistics that can deal with censored data to derive the coefficients. For the non-partial correlations, we used the ASURV software package (Lavalley, Isobe & Feigelson 1992) which only provides Spearman's ρ and Kendall's τ correlation correlation coefficients. For the PCA, we only use the Kendall's partial τ correlation statistics (Akritas & Siebert 1996).

Table 6. The RMS values of residuals after regression from different variables.

Independent variables	Dependent variable	RMS values
l_ν (2500 Å)	EW(C IV)	0.231
α_{ox}	EW(C IV)	0.228
l_ν (2500 Å)+ α_{ox}	EW(C IV)	0.217
EW(C IV)	l_ν (2500 Å)	0.747
α_{ox}	l_ν (2500 Å)	0.645
EW(C IV)+ α_{ox}	l_ν (2500 Å)	0.615

Note. — To consistently compare the RMS values, we compute them using the combined sample without the censored data.

Table 7. Correlation and regression analysis for EW, emission line luminosity, and flux data between Fe K α and C iv.

Relations	$\rho(P)^1$	k^2
EW	0.319(0.027)	0.291 \pm 0.131
$L(\text{line})$	0.529(<0.001)	0.588 \pm 0.079
$f(\text{line})$	0.551(<0.001)	0.978 \pm 0.188

¹Correlations are tested using Spearman's ρ and the significance level (P) is evaluated against the null hypothesis.

²We use the Buckley-James method to do linear regression and k is the slope. The computation is done using the ASURV software package (Lavalley, Isobe & Feigelson 1992)